Modeling damage accumulation during ground-motion sequences for portfolio seismic loss assessments

Salvatore Iacoletti [a],[*], Gemma Cremen [a], Carmine Galasso [a],[b]

[a] *Department of Civil, Environmental and Geomatic Engineering, University College London, Chadwick Building, Gower Street, London, W1CE 6DE, UK*
[b] *Scuola Universitaria Superiore (IUSS), Pavia, Italy*

ARTICLE INFO

ABSTRACT

Conventional earthquake risk assessments use fragility and vulnerability models that are based on seismic demands from individual (mainshock) ground motions, and implicitly assume that a structure is intact before an earthquake hits. This study develops a suite of more realistic state-dependent seismic fragility and vulnerability models for a wide range of building taxonomies, leveraging state-of-the-art methods to account for dynamic damage accumulation in structures due to multiple earthquake events (i.e., ground-motion sequences). Models are developed for 561 building classes (i.e., structural types) from the Global Earthquake Model's global database of fragility and vulnerability models. Four 2010–2012 Canterbury sequence earthquakes are then used to demonstrate an application of the developed models within a portfolio loss assessment, capturing the time-dependent nature of damage and loss in the vulnerability calculations. The results of this application indicate that accounting for damage accumulation across a series of events can significantly increase expected loss ratios compared to a conventional mainshock-only portfolio risk analysis. This work can help analysts to develop and apply state-dependent fragility and vulnerability models for quantifying the potential impact of damage accumulation in portfolio-scale seismic loss assessments.

1. Introduction

Recent worldwide earthquake events have highlighted the need to account for the effects of sequential earthquake-induced ground shaking in both seismic hazard analysis and risk calculations. For instance, studies suggest that the progressive damage of buildings during the entire 2010–2012 Canterbury New Zealand sequence (consisting of a 7.2 moment magnitude (M_W) mainshock and three significant $M_W \geq 5.9$ aftershocks that occurred five, nine, and 15 months later) contributed more to the overall economic losses than those of the mainshock event alone [e.g., 1–4]. The 2016–2017 Central Italy sequence began with a M_W 6.2 earthquake in August 2016, which was followed by two earthquakes (M_W 5.9 and 6.5) in October 2016 (considered triggered events; [5]). After the August 2016 event, 24% of buildings in Accumoli town had damages ranging from negligible to heavy, and 4% collapsed. Most partially damaged buildings in the town suffered additional damage in the two events of October 2016, increasing the total percentage of collapsed buildings to 65% [6].

The vast majority of available numerical fragility and vulnerability models are not suitable for capturing the damage and loss that can accumulate during sequential earthquake events, as they only consider structural demands of individual (mainshock) ground motions on buildings models that are assumed to be initially intact [e.g., 7–10]. Modeling the damage susceptibility of buildings subjected to ground-motion sequences requires state-dependent (or damage-dependent) fragility models, which define the probability that an initially damaged structure (due to a first ground motion) will reach or exceed a certain ith damage state (ds_i) following a subsequent ground motion of a prescribed intensity [e.g., 11,12].

The importance of incorporating aftershock effects in damage and loss modeling has been recognized and increasingly acted upon in more recent years [e.g., 13–15]. Luco et al. [16] investigated the residual capacity of a mainshock-damaged three-story steel moment-resisting frame building adopting back-to-back incremental dynamic analysis (IDA; [17]), in which the same record is applied to represent both a mainshock and an aftershock ground motion. Specifically, a given record is first scaled to induce a target damage level (i.e., reach a prescribed level of maximum interstory drift ratio), then the record is applied again and scaled incrementally to calculate the post-mainshock residual capacity of the structure (i.e., the smallest spectral acceleration that would induce collapse in an aftershock). Using a similar method, Raghunandan et al. [18] computed aftershock fragility models

---

* Corresponding author.

E-mail addresses: salvatore.iacoletti.19@ucl.ac.uk (S. Iacoletti), g.cremen@ucl.ac.uk (G. Cremen), c.galasso@ucl.ac.uk (C. Galasso).

conditional on the mainshock damage. Non-linear dynamic analyses procedures (such as IDA or Multi-Stripe Analysis, MSA) involve significant computational effort [19], site-specific hazard-consistent record selection [e.g., 20,21], and excessive scaling of the seed records to various intensity levels (leading to ground-motion characteristics that do not represent the corresponding intensity level; e.g., [22]).

The cloud approach to seismic structural response quantification [23] is generally considered more appropriate for seismic risk assessments of building portfolios [e.g., 12]. The original cloud analysis approach (i.e., considering only a single ground motion; [23]) uses univariate linear regression (in log scale) of an engineering demand parameter (EDP) on a ground-motion intensity measure (IM). One advantage of the cloud approach is that it does not necessarily require a site-specific, hazard-consistent record selection [e.g., 24], and is based on no-to-moderate scaling of ground motions to describe a (possibly uniform) wide range of IM values [e.g., 25,26].

Some recent work has extended cloud analysis to the prediction of cumulative damage due to aftershocks, but only considering a limited number of building types [e.g., 12,27,28] rather than the wide range of building taxonomies that would be necessary for building portfolio analyses. These studies often only focus on the collapse limit state and generally do not derive vulnerability models that can be used in loss estimation exercises [e.g., 27,28]. In addition, they rely on ground-motion selection procedures based on random sampling approaches such as Latin Hypercube Sampling [e.g., 12,29], which do not necessarily cover a wide uniform range of IMs that may be important for fully capturing the cumulative damage effects of multiple earthquakes.

Furthermore, most studies on the residual capacity of mainshock-damaged buildings and related fragility model development have used peak structural response quantities like maximum displacement or interstory drift ratio as the EDP [e.g., 30–33]. However, Gentile and Galasso [28] demonstrated that this approach may not appropriately capture damage accumulation. This is because peak response quantities may not monotonically increase with the duration and number of the applied ground motions, depending on the accuracy of non-linear hysteretic models (i.e., their ability to adequately capture cyclic and in-cycle stiffness and strength deterioration) and the intensity of the ground motions. Gentile and Galasso [28] introduced a new energy-based framework for more accurately capturing accumulated damage, but this has only been demonstrated on a limited number of archetype reinforced concrete structures and deteriorating ordinary bridges [34], to date.

The aim of this study is to develop a large suite of state-dependent fragility and vulnerability models for a wide range of building taxonomies that might feature in a building portfolio, using a harmonized end-to-end methodology. The methodology leverages the newly developed energy-based framework for state-dependent fragility models by Gentile and Galasso [28], includes a collapse probability model, and incorporates a new standardized procedure to select ground motions with a wide-ranging uniform distribution of IMs. Using 1200 artificial ground-motion pairs, state-dependent fragility and vulnerability models are developed for 561 building classes (i.e., structural types) from the global database provided by the Global Earthquake Model (GEM; [10]) and are shared on a GitHub repository (see Data Availability). This study also discusses an approach for using the developed state-dependent fragility and vulnerability models to quantify both damage and loss accumulation of building portfolios during ground-motion sequences. This approach is illustrated using ground motions from the 2010–2012 Canterbury sequence and a portfolio of building classes representative of the Christchurch central business district.

This study is organized as follows. Section 2 outlines the methodology for developing state-dependent fragility and vulnerability models. Section 3 applies this methodology to develop a global database of fragility and vulnerability models for 561 building classes. Finally, Section 4 introduces an approach to implement the developed state-dependent fragility and vulnerability models in a portfolio loss assessment, before some concluding remarks (Section 5).
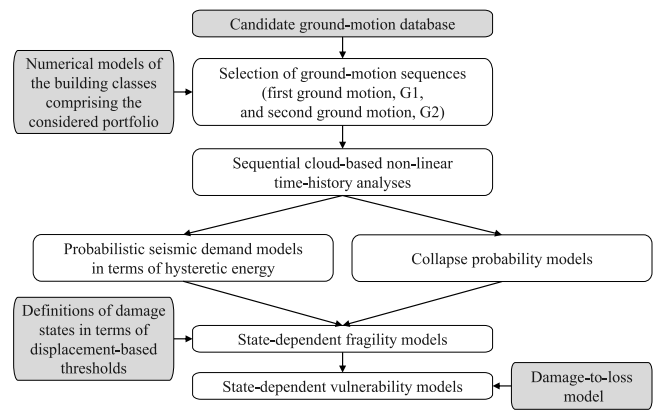

Fig. 1. Flowchart of the proposed methodology. Grey boxes denote the inputs of the methodology.

2. Methodology for state-dependent model development

Fig. 1 shows a flowchart of the underlying end-to-end methodology for state-dependent fragility and vulnerability model development, given a set of building classes (and corresponding numerical models) that might be featured in a building portfolio of interest. The numerical models can be both single- (SDoF) or multi-degree-of-freedom (MDoF) models.

A number of scaled ground-motion pairs (first ground motion, G1, and second ground motion, G2) are defined based on an input candidate ground-motion database and the characteristics of the building classes. This study considers G1 and G2 as two generic ground motions (i.e., they could represent foreshock–mainshock, mainshock–mainshock and mainshock–aftershock combinations), as opposed to most similar studies in the literature that only account for mainshock–aftershock sequences [e.g., 35]. Non-linear time-history analyses are then performed, subjecting the structural models of the building classes to each defined ground-motion pair. The probability of exceeding a set of input ds_i during G2 is estimated through cloud analysis [23] and the recently proposed hysteretic energy-based probability seismic demand model (PSDM; [28]). ds_i are defined in terms of displacement-based thresholds, then converted to energy-based ones using the developed PSDM. The probability of collapse is also considered within the state-dependent fragility model development. State-dependent vulnerability models are then developed using damage-to-loss models (DLMs) that associate each considered ds_i to a corresponding probability distribution of loss ratio [e.g., 36].

The use of ground-motion pairs to develop state-dependent fragility and vulnerability models is consistent with the Markovian assumption [11], which states that the additional damage experienced in a given earthquake only depends on the state of the structure right before the seismic event occurs, rather than the sequence of events that preceded it [37]. This assumption – which is not new in the context of modeling damage accumulation during earthquake sequences [e.g., 11,38] – greatly simplifies the development of both state-dependent fragility and vulnerability models, as well as their implementation in portfolio risk assessments (Section 4).

The following sections present the details of each step of the proposed methodology. The related computer codes are developed in Python (see Data Availability).

2.1. Ground-motion selection

Pairs of unscaled records (G1$_{uns}$ and G2$_{uns}$) are selected from the input candidate ground-motion database and corresponding scaling factors (SF_{G1} and SF_{G2}) are defined. For each set of scaled G1 =

$SF_{G1}G1_{uns}$ and G2 = $SF_{G2}G2_{uns}$ records, a discrete two-dimensional distribution with H bins along the IM_{G1} and IM_{G2} axes (up to a maximum value, IM_{max}) is computed (see Fig. 2). The simulated annealing method (i.e., dual annealing; [39,40]) is used to ensure these distributions uniformly cover the required range of IM_{G1} and IM_{G2} as best as possible. This method minimizes the following objective function:

$$\ln\left[\frac{1}{H}\sum_{p=1}^{H}\left(h_p - \frac{\sum_{p=1}^{H} h_p}{H}\right)^2\right] \qquad (1)$$

where h_p is the number of ground motions falling in the pth two-dimensional bin. Eq. (1) represents the (log) mean squared error of h_p with respect to its average. The simulated annealing method is run with the following constraints:

(1) Values of SF_{G1} and SF_{G2} must strictly lie within [0.5,2.0], so that G1$_{uns}$ and G2$_{uns}$ are only moderately scaled, limiting potential bias in the fragility parameters [e.g., 41,42];

(2) Each unique G1$_{uns}$-G2$_{uns}$ pair can only be selected once;

(3) At least x% of records selected for a given ground motion (G1$_{uns}$ or G2$_{uns}$) must be unique. This constraint helps towards achieving statistical independence of the data points used for fitting the PSDM. The higher the value of x, the greater the computational time needed to minimize Eq. (1). Based on a number of trials with the candidate ground-motion database for state-dependent model development described in Section 3.1.2, $x = 70$ was found to yield an adequate trade-off between excessive computational time and an adequate ground-motion selection for most explored cases, so this value is adopted herein;

(4) Unless the considered structural models are three-dimensional, a G1$_{uns}$-G2$_{uns}$ pair cannot include horizontal components from the same three-component ground-motion record [25]. For one- and two-dimensional structural models, this constraint also helps towards achieving statistical independence of the data points used for fitting the PSDM.

The proposed ground-motion selection procedure requires input values for H and IM_{max}. $H = 20$ is recommended for application of the methodology (and used in this work), to provide a reasonable discretization of IM levels. IM_{max} should be selected such that each considered ds_i may be reached for G1 [e.g., 25], but its value is often further constrained by the limitations of the records in the input candidate ground-motion database (see Section 3.1.2). Input structural models are grouped together according to their fundamental periods and ductility (see 3.2.1), where each group is associated with one IM and a corresponding IM_{max} value. The ground-motion selection procedure is then carried out for each relevant $\{IM, IM_{max}\}$ combination.

Fig. 2 compares the proposed ground-motion selection procedure (lower panel) with the randomized approach based on Latin Hypercube Sampling used in Aljawhari et al. [12] (upper panel), for $IM_{max} = 2g$. The candidate ground-motion database for state-dependent model development described in Section 3.1.2 is used for both examples. A significant number of ground motions are concentrated at lower IM values in the upper plot. This is because the ground-motion database in Section 3.1.2 includes a large proportion of records with relatively low IMs; thus, a randomized G1-G2 pair selection is less likely to select large $IM_{G1} - IM_{G2}$ pairs. The lower panel in Fig. 2 displays reasonably uniform distributions of $IM_{G1} - IM_{G2}$ pairs between 0 and 2 g.

The IM type used in this work is the average spectral acceleration at a range of periods of interest (AvgSA(0.2T–1.5T), henceforth referred to as AvgSA(T)), conventionally computed as the geometric mean of 10 discrete evenly-spaced spectral ordinates between 0.2T and 1.5T [e.g., 43], where T is the fundamental period of the considered structure. AvgSA is relatively more sufficient [44] than other IMs, which means that site-specific, hazard-consistent ground-motion selection [e.g., 24] is relatively less crucial for cloud analysis [e.g., 45, 46].

In summary, the proposed ground-motion selection procedure compiles artificial ground-motion pairs by moderately scaling ground-motion records in a uniform exploration of the $IM_{G1} - IM_{G2}$ space. The resulting state-dependent fragility and vulnerability models can be used under multiple ground-motion sequences that could occur in the form of multiple mainshocks, mainshocks triggering additional earthquakes on nearby fault segments, mainshock–aftershock and aftershock–aftershock sequences. Real ground-motion sequences could be considered instead [e.g., 35,47–49]. However, since recordings of sequences with high intensities are generally scarce, using real data would limit our ability to calibrate the models with observations of significant damage accumulation and jeopardize the statistical robustness of the models. Furthermore, the proposed procedure does not rely on site-specific hazard-consistent record selection methodologies [e.g., 21, 35], making it relevant for large-scale (e.g., global) applications [10].

2.2. Probabilistic seismic demand model

Non-linear time-history analyses are performed for each input numerical model and each selected G1–G2 pair, incorporating a number of seconds of free vibration in between the ground motions. This free-vibration time allows the structure to come to the rest position after G1, and it can be selected based on the fundamental period of the considered structure and engineering judgement. A free vibration time of 40 s is used in this work, which is reasonable for all building classes considered as part of the state-dependent model development process in Section 3 and widely accepted in the literature [e.g., 12,28].

The vector-valued PSDM developed by Gentile and Galasso [28] describes the structural demands obtained from the non-linear time-history analyses using the cumulative hysteretic energy dissipated in the ground-motion sequence (i.e., G1 and G2) as the EDP. This PSDM is the first physically-consistent model that accounts for the accumulation of damage, even though it is solely based on numerical analyses and requires further validation through experimental/field data. It is expressed as:

$$E_H = E_{H,G1} + E_{H,G2} = a\theta_{G1}^b + \left(1 - m\theta_{G1}\right)c_0 IM_{G2}^d \qquad (2)$$

in which E_H is the cumulative hysteretic energy associated with G1 and G2, $E_{H,GN}$ is the hysteretic energy associated with ground motion GN (where N is either 1 or 2), θ_{G1} is the maximum displacement (or drift) associated with G1, and IM_{G2} is as defined previously. All other variables (a, b, c_0, d, and m) are parameters estimated through regression. Eq. (2) with (a) $IM_{G2} = 0$ is the power-law relationship $E_H = E_{H,G1} = a\theta_{G1}^b$, which can be calibrated with G1 data only; and (b) $\theta_{G1} = 0$ is the power-law relationship $E_H = E_{H,G2} = c_0 IM_{G2}^d$, which is commonly adopted for cloud-based single-ground-motion (e.g., mainshock) problems. The power-law relationship $E_H = E_{H,G2} = c_0 IM_{G2}^d$ can be calibrated using G1 data only because G1 can be interpreted as a G2 that follows a G1 producing zero drift [28]. The factor $\left(1 - m\theta_{G1}\right)$ linearly reduces the intercept of the $E_{H,G2} = c_0 IM_{G2}^d$ relationship. The steps used to fit Eq. (2) are similar to those described in Gentile and Galasso [28]:

1. Fit the relationship $E_{H,G1} = a\theta_{G1}^b$ through linear least-squares regression in the log–log space, using G1 data only (i.e., θ_{G1}, $E_{H,G1}$);

2. Fit the relationship $E_{H,G2} = c_0 IM_{G2}^d$ through linear least-squares regression in the log–log space using G1 data only (i.e., IM_{G1}, $E_{H,G1}$);

3. Determine the parameter m from $E_{H,G2} = \left(1 - m\theta_{G1}\right)c_0 IM_{G2}^d$ though non-linear least-squares regression in the log–log space, using θ_{G1}, IM_{G2}, and $E_{H,G2}$.
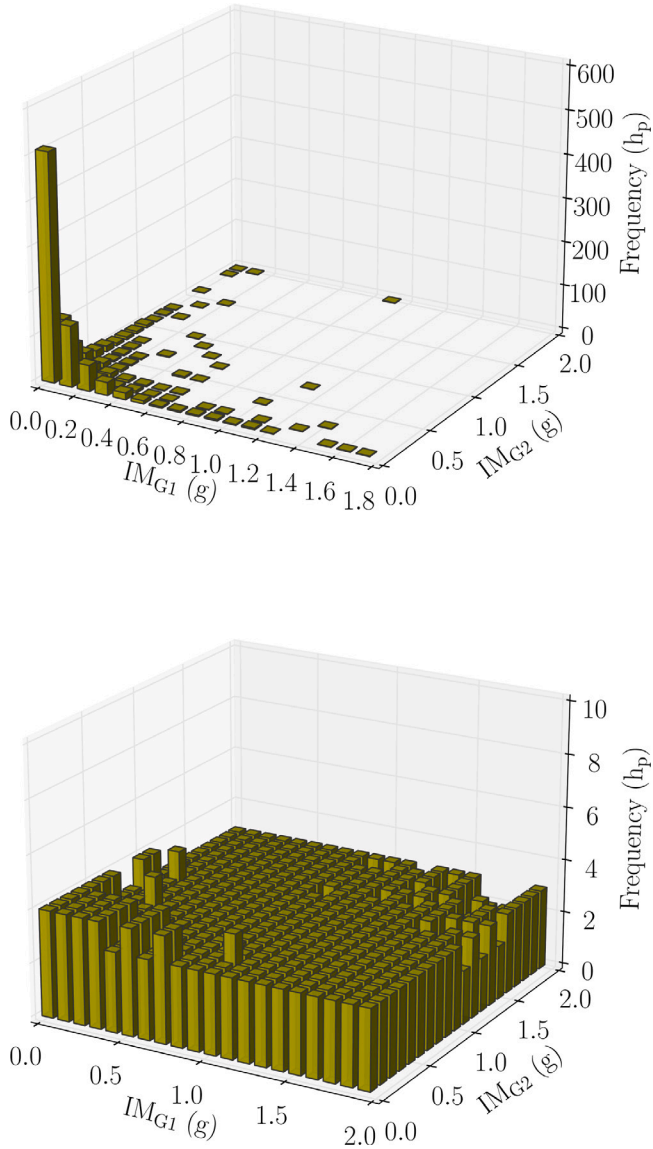
Fig. 2. Comparing two procedures for selecting ground-motion pairs (G1-G2) with IM values between 0 and 2 g, from the candidate ground-motion database described in Section 3.1.2. Upper panel: the histogram of G1-G2 obtained from the selection procedure specified in Aljawhari et al. [12]. Lower panel: distributions of G1-G2 obtained from the selection procedure proposed in this work. The average number of ground motions falling in the pth 2D bin is equal to $\sum_{p=1}^{H} h_p/H$, with H bins along the IM_{G1} and IM_{G2} axes.

Step #3 represents a departure from the corresponding step in Gentile and Galasso [28], which uses non-linear least squares regression in linear space to calibrate m. The modification to Step #3 is made because it is found that the log-space residuals of $E_{H,G2} = (1 - m\theta_{G1}) c_0 IM_{G2}^d$ for the data of Section 3 are closer to a normal distribution than those in linear space, based on the Euclidean metric distance proposed by Chun et al. [50]. For practical implementation of the above steps, Eq. (2) is calibrated excluding data that result in (a) $E_{H,G1} = 0$ or $E_{H,G2} = 0$, as these represent cases where the structure does not incur any damage (i.e., linear elastic conditions); and (b) collapse, according to the details of Section 2.3.

2.3. Collapse probability model

In this study, collapse corresponds to a global dynamic instability of the numerical analysis (i.e., non-convergence) or the exceedance of

a conventional maximum displacement [e.g., 10] during G1 or G2. The probability of collapse $P(C \mid DS_{G1}, IM_{G2})$ (where DS_{G1} corresponds to a damage state experienced during G1) is modeled with a formulation of the generalized logistic function [51], in which θ_{G1} and IM_{G2} are predictors (consistent with Eq. (2)):

$$P(C \mid DS_{G1}, IM_{G2}) = A + \frac{1 - A}{\left[1 + \left(\sqrt{1 - \frac{\theta_{G1}}{\theta_{G1}^*}}\right) e^{-(\kappa + \delta \ln IM_{G2})}\right]}$$

$$A = \frac{1}{(1 + e^{-(\alpha + \gamma \ln \theta_{G1})})} \tag{3}$$

α, γ, κ, and δ are model parameters, and θ_{G1}^* is the lowest value of θ_{G1} that results in $P(C \mid DS_{G1}, IM_{G2}) = 1$ (i.e., corresponding to A approaching 1 in Eq. (3)). Eq. (3) represents a univariate logistic regression model dependent on θ_{G1} in the $\theta_{G1} - P(C \mid DS_{G1}, 0)$ plane, and a univariate logistic regression model dependent on IM_{G2} in the $IM_{G2} - P(C \mid 0, IM_{G2})$ plane (which is consistent with the logistic function commonly adopted for cloud-based single-ground-motion problems). Based on these observations and consistent with the PSDM proposed by Gentile and Galasso [28], the following steps are used to fit Eq. (3):

1. Set $IM_{G2} = 0$ in Eq. (3), leading to $P(C \mid DS_{G1}, 0) = A = 1/(1 + e^{-(\alpha + \gamma \ln \theta_{G1})})$. Determine the parameters α and γ via logistic regression using G1 data only (i.e., θ_{G1});
2. Set $\theta_{G1} = 0$ in Eq. (3), leading to $P(C \mid 0, IM_{G2}) = 1/(1 + e^{-(\kappa + \delta \ln IM_{G2})})$. The parameters κ and δ are estimated using G1 data only (i.e., IM_{G1}), in line with the logic followed in Section 2.2.

2.4. State-dependent fragility models

State-dependent fragility models for different combinations of damage states due to G1 (i.e., DS_{G1}) and G1+G2 (i.e., DS_{G1+G2}) are denoted as $P\left(DS_{G1+G2} \geq ds_i \mid DS_{G1}, IM_{G2}, NoC\right)$, representing the probability of exceeding the ith damage state (ds_i, with $i = DS_{G1}, \ldots, n_{DS}$ and n_{DS} equal to the number of considered damage states) due to G1+G2, conditioned on DS_{G1}, IM_{G2} and no collapse (i.e., NoC). The fragility model can be expressed as:

$$P\left(DS_{G1+G2} \geq ds_i \mid DS_{G1}, IM_{G2}, NoC\right) = \Phi\left(\frac{\mu_{\ln E_H \mid DS_{G1}, IM_{G2}, NoC}}{\beta_{\ln E_H \mid DS_{G1}, IM_{G2}, NoC}}\right)$$

$$\tag{4}$$

in which Φ is the standard normal cumulative distribution function, $\mu_{\ln E_H \mid DS_{G1}, IM_{G2}, NoC}$ is the mean and $\beta_{\ln E_H \mid DS_{G1}, IM_{G2}, NoC}$ is the dispersion of the fragility model. Note that $DS_{G1+G2} \geq DS_{G1}$ (and the right hand-side of Eq. (4) reduces to 1 for $ds_i = DS_{G1}$). If $DS_{G1} = ds_0$ (no damage occurs due to G1), Eq. (4) becomes equivalent to a single-ground-motion fragility model that only considers the possible occurrence of damage due to G2. $\mu_{\ln E_H \mid DS_{G1}, IM_{G2}, NoC}$ and $\beta_{\ln E_H \mid DS_{G1}, IM_{G2}, NoC}$ are computed with the equations provided by Gentile and Galasso [28]. Building-to-building variability ($\sigma_{bld-to-bld}$) is also included in the computation of $\beta_{\ln E_H \mid DS_{G1}, IM_{G2}, NoC}$ as suggested by Martins and Silva [10]. The value of $\sigma_{bld-to-bld}$ can be selected from suitable related literature [e.g., 52]. $\sigma_{bld-to-bld}$ is set equal to 0.3 in this work, per Martins and Silva [10].

The total probability of damage exceedance due to G1+G2 can be expressed as:

$$P\left(DS_{G1+G2} \geq ds_i \mid DS_{G1}, IM_{G2}\right) =$$

$$P(DS_{G1+G2} \geq ds_i \mid DS_{G1}, IM_{G2}, NoC)(1 - P(C \mid DS_{G1}, IM_{G2})) +$$

$$P(C \mid DS_{G1}, IM_{G2}) \tag{5}$$

in which $P(C \mid DS_{G1}, IM_{G2})$ is the probability of collapse calculated with Eq. (3).

Table 1

Taxonomy of the building classes used in the illustrative application. For further details on the capacity curves corresponding to each building class and the SDoF model development, the reader is referred to Martins and Silva [10].

Construction material	Lateral load resisting system	Ductility level	Number of stories
Unreinforced masonry (MUR)	Moment-resisting bare frames (LFM)	Low ductility (DUL)	HX, where X indicates the number (or corresponding range) of stories.
Reinforced masonry (MR)	Infilled frames (LFINF)	Moderate ductility (DUM)	The maximum value of X depends on:
Confined masonry (MCF)	Wall systems (LWAL)	High ductility (DUH)	– construction material
Reinforced concrete (CR)	Dual systems (LDUAL)	Non-ductile (DNO), only for unreinforced	– lateral load system
AdobeL/earthen (MUR-ADO)		masonry structures and earthen	– ductility level
Timber/wood (W)		construction	
Steel (S)			
Composite (SCR)			

2.5. State-dependent vulnerability models

This step of the methodology requires a DLM in the form of expected values, $E(LR \mid DS)$ and (optionally) coefficients of variation, $CoV(LR \mid DS)$, of the loss conditioned on each considered damage state. The DLM is usually region- and building-class-specific, and should be carefully selected based on the considered application [e.g., 53]. Given the time windows in which seismic sequences commonly take place (e.g., a few months to a few years; [54]), repair of damaged buildings between the occurrence of G1 and G2 is neglected in the development of the state-dependent vulnerability models, per Papadopoulos and Bazzurro [15]. These vulnerability models can be written as [e.g., 55]:

$$E(LR \mid DS_{G1}, IM_{G2})$$
$$= \sum_{i=DS_{G1}}^{nDS} \left[P\left(DS_{G1+G2} = ds_i \mid DS_{G1}, IM_{G2}\right) \int_0^1 lr \cdot f\left(lr \mid ds_i\right) \, dlr \right]$$

(6)

in which $P\left(DS_{G1+G2} = ds_i \mid DS_{G1}, IM_{G2}\right)$ is the probability of occurrence of damage state ds_i ($i = DS_{G1}, \ldots, n_{DS}$) given IM_{G2} and the previous damage state DS_{G1} (derived from Eq. (4)), $E(LR \mid DS_{G1}, IM_{G2})$ is the expected loss ratio LR given DS_{G1} and IM_{G2}, and $f\left(lr \mid ds_i\right)$ is the probability density function of LR given ds_i. Eq. (6) could be extended to describe the variability around the expected loss ratio [see 55].

3. State-dependent model development

The methodology is now used to develop state-dependent fragility and vulnerability models for a large database of building classes. This database was developed by GEM based on a worldwide survey and comprises 561 building classes. Single-ground-motion fragility and vulnerability models for each building class have been developed by Martins and Silva [10], and then used for the assessment of economic losses in the global seismic risk model [56]. Each building class is identified following a simple taxonomy (see Table 1; [10]): (1) construction material; (2) lateral load resisting system; (3) ductility level; and (4) height (number of stories). For further details, the reader is referred to Martins and Silva [10].

3.1. Details on the required inputs

3.1.1. Numerical models and damage state definition

Input numerical equivalent non-linear SDoF models [e.g., 57] are developed for each building class, using OpenSees ([58]; see Data Availability). Each SDoF model is associated with a capacity curve provided by Martins and Silva [10] (see Fig. 3), expressed in terms of spectral acceleration (SA) versus spectral displacement (SD). The shape of the capacity curves depends on the expected reduction in
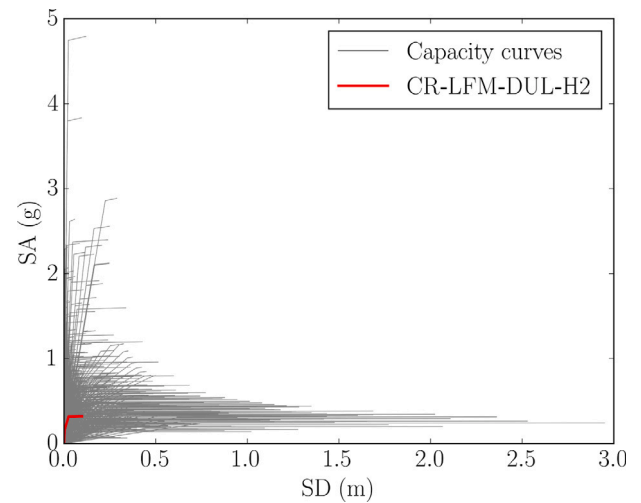

Fig. 3. Capacity curves provided by Martins and Silva [10]. The capacity curve for CR-LFM-DUL-H2 (used in Section 3.2.2) is highlighted in red.

the base shear capacity due to damage accumulation. For building classes where no significant base shear capacity reduction is expected (e.g., steel frames, timber and composite structures), a trilinear elasto-plastic capacity curve is used. For other building classes, the capacity follows a quadrilinear curve (e.g., confined masonry or reinforced concrete with infills). The non-linear hysteretic behavior of the SDoF models is described with the *Pinching4* material in OpenSees, using the cyclic degradation parameters from Martins and Silva [10]. For further details on the SDoF model development, the reader is referred to Martins and Silva [10].
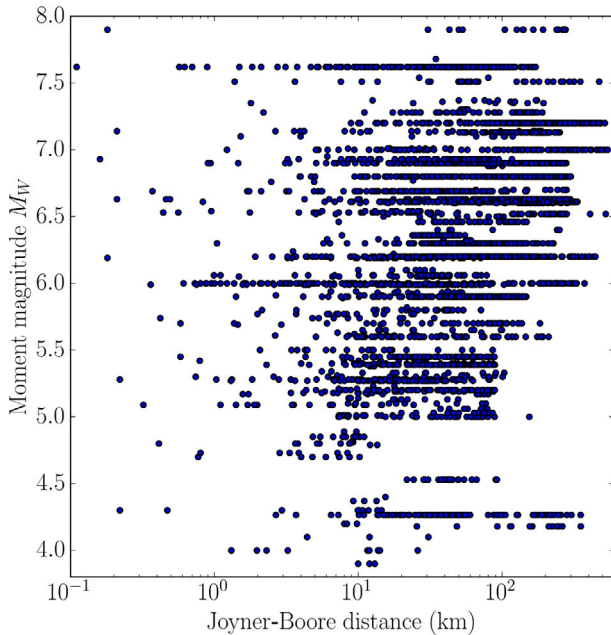
Four building-class-specific ds_i are considered (from slight damage, ds_1, to complete damage, ds_4). ds_i are defined based on the yielding (d_y) and the ultimate (d_u) displacements from the capacity curves (Table 2), which are derived from relevant literature [10]. Each damage-state displacement threshold is modeled with a lognormal distribution to account for aleatory uncertainty in the damage criteria. The median ds_i thresholds ($\overline{\theta_{ds_i}}$) are provided in Table 2, and the coefficient of variation is set equal to 0.45 [10]. The conventional maximum displacement for the definition of collapse (see Section 2.3) is 1.5 times the displacement that results in ds_4 [10]. For further details on the definition of the ds_i, the reader is referred to Martins and Silva [10].

It is acknowledged that SDoF models might not accurately capture the response of individual buildings because they do not account for the effects of ground-motion directionality, aftershock polarity, structural

Table 2
Median damage state thresholds (after Martins and Silva [10]) and description of the ds_i. d_y and d_u are the yielding and the ultimate displacements from the capacity curve, respectively. For further details on the definition of the damage states in terms of d_y and d_u, the reader is referred to Martins and Silva [10].

Damage state	$\overline{\theta_{ds_i}}$	Description
Slight (ds_1)	$0.75d_y$	Non-structural damage only.
Moderate (ds_2)	$0.5d_y + 0.33d_u$	Moderate structural and non-structural damage with no significant yielding of members.
Extensive (ds_3)	$0.25d_y + 0.67d_u$	Severe structural and non-structural damage. Some residual strength and stiffness is retained.
Complete (ds_4)	d_u	Full exploitation of strength and ductility. Very low residual strength and stiffness.

Fig. 4. Moment magnitude versus Joyner–Boore distance scatter plot corresponding to the candidate ground-motion database used for state-dependent model development.

Table 3
Damage-to-loss ratios used in this study (after Martins and Silva [10]).

Damage state	$E(LR \mid DS)$	$CoV(LR \mid DS)$
Slight (ds_1)	0.05	0.30
Moderate (ds_2)	0.20	0.20
Extensive (ds_3)	0.60	0.10
Complete (ds_4)	1.00	0.00

3.1.3. Damage-to-loss model

The DLM in Table 3 is used in this study for illustrative purposes only, in which the loss ratio corresponding to each ds_i follows a beta distribution. This DLM has been used by Martins and Silva [10] to develop single-ground-motion vulnerability models for all building classes considered in this study. The detailed definition of building class-specific DLMs is outside the scope of this study.

3.2. Developing the models

3.2.1. Ground-motion selection

AvgSA(T) are determined by clustering building classes according to ranges of fundamental period values (see Table 4), where each group is assigned an approximate T value. A preliminary maximum AvgSA(T) value for each building class is first calculated as $SA_y R_y + 0.5$, where SA_y is the yielding capacity of the considered building class, R_y is calculated as:

$$R_y = \begin{cases} \sqrt{\mu_d - 1} & T < T_c \\ \mu_d & T > T_c \end{cases} \qquad (7)$$

and μ_d is the ductility of the corresponding numerical model. T_c, the transitional period, is taken to be 1s [65]. Eq. (7) is a conservative version of the strength reduction factor by Chopra [66], but only requires knowledge of T_c. The preliminary values of maximum AvgSA(T) are then rounded up to the nearest 0.5 g unit, to finalize a limited set of maximum AvgSA(T) values across the considered building classes. Maximum AvgSA(T) values are also constrained between 1 g and 3.5 g for $T \leq 0.8$ s, and from 1 g to 3 g for $T > 0.8$ s. Upper limit maximum values of 3.5 g ($T \leq 0.8$ s) and 3 g ($T > 0.8$ s) are compatible with the maximum AvgSA(T) value of the input ground-motion database. 1 g is set as the lower limit of the maximum value, to avoid excessive extrapolation in the fitting of the PSDM (Section 2.2) and the collapse probability model (Section 2.3) [e.g., 25]. Fig. 5 provides the number of building classes in each final grouping, i.e., associated with each combination of assumed T (Table 4) and maximum AvgSA(T).

The procedure detailed in Section 2.1 is run to select 1200 sets of $G1_{uns}$, $G2_{uns}$, SF_{G1}, and SF_{G2} for each building-class grouping. 1200 is deemed an appropriate number of ground-motion pairs to achieve statistically sufficient results in the structural response and is consistent with previous studies [e.g., 12,28].

irregularities, higher mode behavior, localized failures, or the vertical component of earthquake-induced ground motions [e.g., 59,60]. However, SDoF models are generally deemed acceptable for describing the behavior of general building classes in the context of portfolio seismic risk assessments [e.g., 10,61,62], due to the typical lack of available detailed structure-specific data and limits on computational power [61]. Furthermore, using simpler structural modeling assumptions (i.e., SDoF instead of MDoF models) makes it easier to calibrate seismic risk models against real loss data [63].

3.1.2. Candidate ground-motion database

The input candidate ground-motion database consists of 7009 as-recorded three-component ground-motion records of the Pacific Earthquake Engineering Research (PEER) NGA-West2 database [64], which has been used to develop fragility models in several studies [e.g., 10,22]. The horizontal components of each three-component record are considered separately, such that the input database comprises 14018 single-component accelerograms. Fig. 4 provides a moment magnitude (M_W) versus Joyner–Boore distance scatter plot corresponding to the candidate ground-motion database. M_W ranges between 3.9 and 7.9, and the Joyner–Boore distance ranges between 0.1 and 600 km.

Table 4
Period ranges used to associate building classes with an assumed fundamental period (T) to compute AvgSA(T) (see Section 2.1).

Period (s) range for building classes	Assumed T (s)
0–0.1	0.05
0.1–0.3	0.20
0.3–0.5	0.40
0.5–0.7	0.60
0.7–0.9	0.80
0.9–1.25	1.00
1.25–1.75	1.50
>1.75	2.00
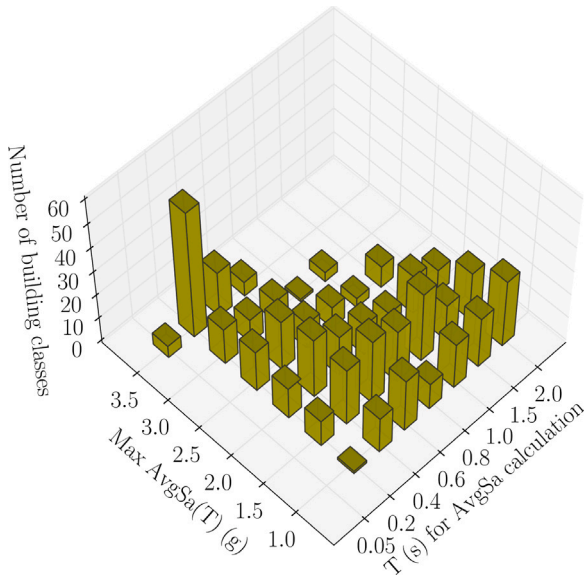
Fig. 5. Number of building classes associated with each combination of assumed T (Table 4) and maximum AvgSA(T).

3.2.2. Additional steps: Example details

This section provides an example application of the rest of the model development methodology to building class CR-LFM-DUL-H2. This building class represents low-ductility buildings with a reinforced concrete frame and two stories (see Table 1) and features in several developed countries worldwide [67]. The capacity curve for CR-LFM-DUL-H2 is highlighted in Fig. 3. The numerical SDoF model for CR-LFM-DUL-H2 has a fundamental period equal to 0.56s. From Section 3.1.2, CR-LFM-DUL-H2 is assigned an assumed period of T=0.6s and a maximum AvgSA(T) value equal to 1.5 g. The selected (moderately scaled) ground motions are shown in Fig. 6, where a wide range of AvgSA(T) values are observed for both G1 and G2.

Fig. 7 provides the calibrated PSDM and collapse probability model for CR-LFM-DUL-H2. Fig. 7 shows that when the conventional maximum displacement of collapse for CR-LFM-DUL-H2 is exceeded (i.e., $\theta_{G1} \gtrsim 0.15$), the collapse probability model is correctly equal to 1. As expected, the probability of collapse increases with increasing θ_{G1} (i.e., increasing the initial DS_{G1}) and increasing IM_{G2}.

Fig. 8 provides state-dependent fragility models developed for CR-LFM-DUL-H2 (the corresponding approximate mean, $\mu_{\ln E_H | DS_{G1}, AvgSA_{G2}(0.6\ s)}$, and dispersion, $\beta_{\ln E_H | DS_{G1}, AvgSA_{G2}(0.6\ s)}$, are presented in Table 5). As expected, $\mu_{\ln E_H | DS_{G1}, AvgSA_{G2}(0.6\ s)}$ decreases with increasing DS_{G1} (e.g., the mean of the model for $ds_4 \mid ds_3$ is lower than that for $ds_4 \mid ds_2$). Fig. 9 provides the state-dependent vulnerability models for CR-LFM-DUL-H2, based on the fragility models shown in Fig. 8. As expected, $E(LR \mid DS_{G1}, AvgSA_{G2}(0.6\ s))$ increases for increasing DS_{G1}. For instance, $E(LR \mid DS_{G1}, AvgSA_{G2}(0.6\ s) = 1\ g)$
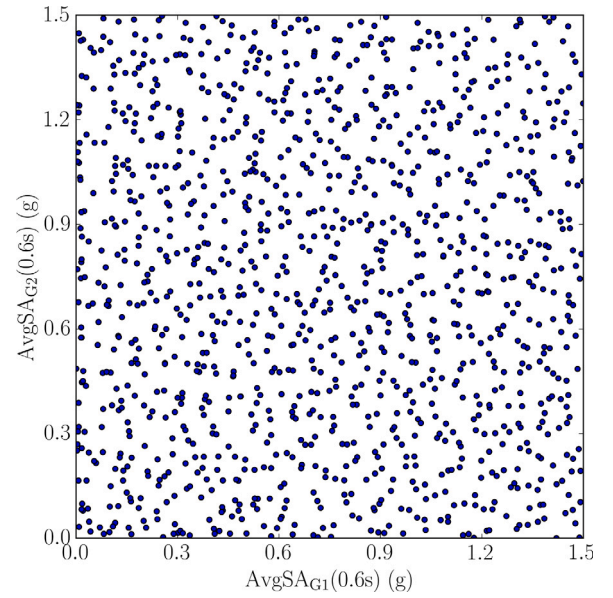

Fig. 6. 2D scatter plot of AvgSA$_{G1}$(0.6s) and AvgSA$_{G2}$(0.6s) for CR-LFM-DUL-H2 and a maximum AvgSA(0.6s) value of 1.5 g.
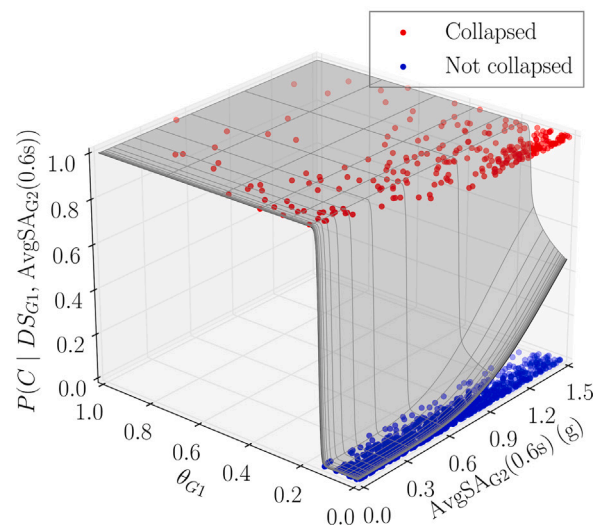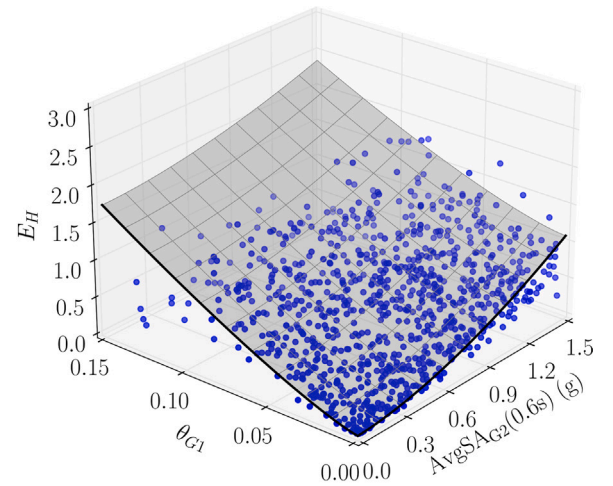

Fig. 7. Probabilistic seismic demand model (upper panel) and collapse probability model (lower panel) for CR-LFM-DUL-H2.
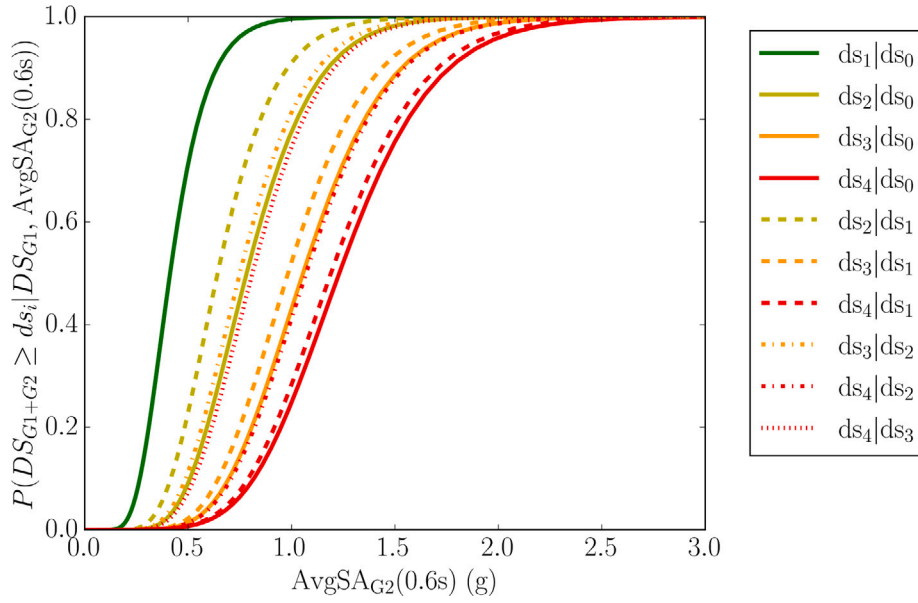
Fig. 8. State-dependent fragility models (indicated with $DS_{G1+G2} \mid DS_{G1}$) for CR-LFM-DUL-H2.

Table 5

$\mu_{\ln E_H \mid DS_{G1}, AvgSA_{G2}(0.6s)}$, and $\beta_{\ln E_H \mid DS_{G1}, AvgSA_{G2}(0.6s)}$ of the state-dependent fragility models (indicated with $DS_{G1+G2} \mid DS_{G1}$) for CR-LFM-DUL-H2.

	$\mu_{\ln E_H \mid DS_{G1}, IM_{G2}}$ (g)	$\beta_{\ln E_H \mid DS_{G1}, IM_{G2}}$
$ds_1 \mid ds_0$	0.413	0.340
$ds_2 \mid ds_0$	0.780	0.327
$ds_3 \mid ds_0$	1.049	0.307
$ds_4 \mid ds_0$	1.222	0.299
$ds_2 \mid ds_1$	0.642	0.334
$ds_3 \mid ds_1$	0.978	0.311
$ds_4 \mid ds_1$	1.182	0.299
$ds_3 \mid ds_2$	0.748	0.327
$ds_4 \mid ds_2$	1.063	0.303
$ds_4 \mid ds_3$	0.808	0.321

Fig. 9. State-dependent vulnerability models for CR-LFM-DUL-H2.

is 9.5%, 52.5%, 106.1% greater than the single-ground-motion case (i.e., $DS_{G1} = ds_0$) when DS_{G1} is ds_1, ds_2, and ds_3, respectively.

4. Application to portfolio loss assessment

4.1. Proposed implementation procedure

This section details a procedure for using the developed state-dependent fragility and vulnerability models to quantify both damage and loss accumulation during ground-motion sequences. The procedure is shown in Fig. 10 for one asset (with known location and building class); this process would be repeated for all assets of interest. It is assumed that the IMs of all N_e events in the sequence are known at the asset's location. IM values are generally available for past earthquakes at station sites [e.g., 68], otherwise they can be computed with simulation-based approaches [e.g., 69]. The procedure involves an iteration through N_r realizations to sample different damage states of the asset after each ground motion. Each realization comprises of the following steps:

- Set the current damage state and expected loss ratio to the respective values associated with the asset prior to the considered ground motion or sequence, i.e., $DS_{cur} = DS_{orig} = DS_{G1}$ and $E(LR^{cur}) = E(LR^{orig}) = E(LR \mid DS_{cur}, 0)$. If the prior state of the asset is unknown, it is assumed that $E(LR^{cur}) = 0$ and $DS_{cur} = ds_0$;
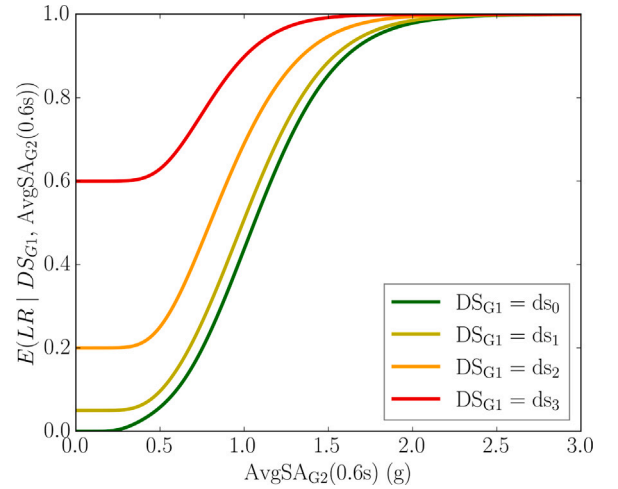
- For the ground motion of the eth event in the considered sequence (IM_{G2}):

  1. Calculate the updated expected loss ratio $E(LR^{upd}) = E(LR \mid DS_{cur}, IM_{G2})$;
  2. Sample an updated damage state ($DS_{upd} = DS_{G1+G2} \geq DS_{cur}$) based on the values of $P(DS_{G1+G2} \geq ds_i \mid DS_{cur}, IM_{G2})$;
  3. Update $DS_{cur} = DS_{upd}$;
  4. If $E(LR^{upd}) > E(LR^{cur})$, then save the eth expected LR increment for the rth realization as $E(\Delta LR_{e,r}) = E(LR^{upd}) - E(LR^{cur})$;

- The total expected loss ratio increase for the rth realization is computed as: $E(\Delta LR_r) = \sum_{e=1}^{N_e} E(\Delta LR_{e,r})$.

The final expected loss ratio for the asset is computed as $E(LR) = \sum_{r=1}^{N_r} E(\Delta LR_r) + E(LR^{orig})$. Note that the event-specific expected increase in LR, $E(\Delta LR_e)$, can be computed as $E(\Delta LR_e) = \frac{1}{N_r} \sum_{r=1}^{N_r} E(\Delta LR_{e,r})$.
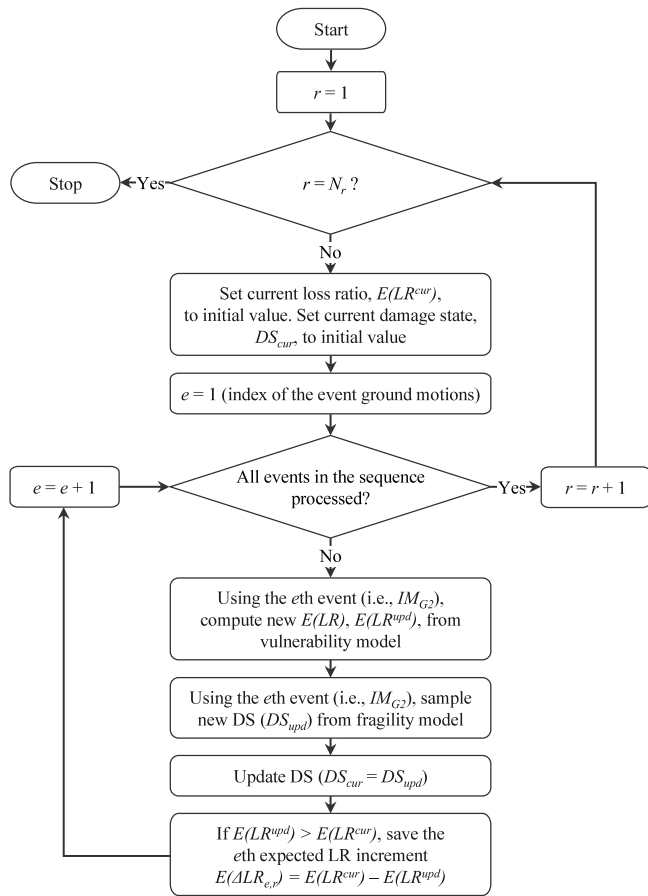
Fig. 10. Proposed procedure for using the developed state-dependent fragility and vulnerability models to quantify both damage and loss accumulation during ground-motion sequences, for a single asset.

Table 6

$E(\Delta LR_e)$ and $E(LR)$ for CR-LFM-DUL-H2 during the 2010–2012 Canterbury sequence. AvgSA(0.6 s) values of the four considered earthquakes from the 2010–2012 Canterbury sequence are reported in parentheses.

	Proposed approach	Alternative approach #1	Alternative approach #2
$E(\Delta LR_e)$ M_W 7.2 mainshock (0.65 g)	0.127	0.127	0.127
$E(\Delta LR_e)$ M_W 6.2 aftershock (0.94 g)	0.390	N/A	0.376
$E(\Delta LR_e)$ M_W 6.0 aftershock (0.54 g)	0.147	N/A	0.071
$E(\Delta LR_e)$ M_W 5.9 aftershock (0.50 g)	0.023	N/A	0.058
$E(LR)$	0.687	0.127	0.633

4.2. Example implementation

This section presents a simple case study – set in Christchurch, New Zealand at the time of the 2010–2012 Canterbury sequence – to illustrate the implementation procedure proposed in Section 4.1. The building classes used for the case-study portfolio are selected based on the findings of Uma et al. [70], which reports that the four predominant building typologies in the Christchurch central business district at the time of interest were:

- Wood frames (W-LFM in Table 1) representing around 30% of the total number of buildings;
- Concrete frames (CR-LFM in Table 1) representing around 23% of the total number of buildings;
- Unreinforced masonry (MUR-LWAL in Table 1) representing around 36% of the total number of buildings;
- Reinforced masonry (MR-LWAL in Table 1) representing around 11% of the total number of buildings.

75% of W-LFM, CR-LFM and MR-LWAL building typologies are assumed to have limited ductility (DUL) and 25% are assumed to have moderate ductility (DUM). This is because, at the location and time of interest, there were (a) more buildings predating seismic regulations (i.e. built in the first half of the 20th century), which are expected to have had only limited ductility; and (b) other buildings could have potentially lacked ductile detailing [70]. MUR-LWAL is always considered non-ductile (DNO in Table 1). For all building-typologies, building height is equally distributed between a low-rise story range (denoted as H2, 1–3 stories; [70]), and a mid-rise story range (denoted as H5, 4–7

stories; [70]). The building classes of the case-study portfolio are shown in Fig. 11; all correspond to building classes for which state-dependent fragility and vulnerability models were developed in Section 3.

The case-study sequence consists of ground motions from four earthquakes of the 2010–2012 Canterbury sequence. These four events are the mainshock (M_W 7.2 Darfield earthquake) and three aftershocks (M_W 6.2, M_W 6.0, and M_W 5.9, respectively). The response spectra are downloaded from the GeoNet website (see Data Availability) at the Christchurch Resthaven (REHS) station [68], which is located in the Christchurch central business district (longitude: 172.635°; latitude: −43.522°) and is characterized by site class D (deep or soft soil) as defined by the New Zealand Loadings Standard [71]. For convenience, it is assumed that all assets in the case-study portfolio are located at this site.

$E(\Delta LR_e)$ and $E(LR)$ are calculated for each building class according to the approach outlined in Section 4.1 (henceforth called the proposed approach), and compared with values obtained using two alternative approaches:

- The conventional approach used in seismic risk assessments (henceforth called alternative approach #1), which uses the single-ground-motion vulnerability model (i.e., $E(LR^{upd}) = E(LR \mid 0, IM_{G2})$) to compute $E(\Delta LR_{MS,r})$ for the mainshock event ground motion (MS) only, such that $E(\Delta LR_e) = \frac{1}{N_r} \sum_{r=1}^{N_r} E(\Delta LR_{MS,r})$;
- A single-ground-motion approach that also considers aftershocks (henceforth called alternative approach #2). In this case, the underlying vulnerability calculations do not account for damage accumulation (i.e., the vulnerability module has no memory of the previous damage state). For this approach, $E(\Delta LR_e)$ is evaluated independently with the single-ground-motion vulnerability model (i.e., $E(LR^{upd}) = E(LR \mid 0, IM_{G2})$) for each event and $E(\Delta LR_e)$ is computed accordingly.

Table 6 reports $E(\Delta LR_e)$ and $E(LR)$ for the case-study portfolio building class CR-LFM-DUL-H2 highlighted in Section 3.2.2, along with IM_{G2} = AvgSA(0.6s) values corresponding to the four considered ground motions. Table 7 provides the $E(LR)$ values for all building classes of the case-study portfolio. From this table, the proposed approach produces $E(LR)$ values two to 20 times higher than alternative approach #1. This is at least partially explained by the fact that the first aftershock (M_W 6.2) produces larger IM values than the mainshock (see Table 6). The neglect of damage accumulation in alternative approach #2 can provide misleading $E(LR)$ values (including $E(LR) > 1$), which may be either lower and higher than those of the proposed approach (see Tables 6 and 7).

5. Conclusions

This study develops state-dependent fragility and vulnerability models for a wide range of globally applicable building taxonomies, using
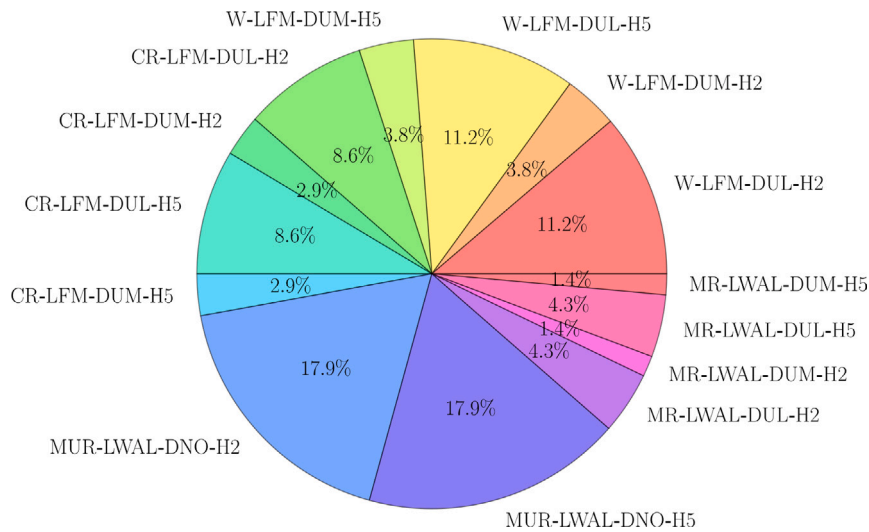
Fig. 11. Building classes of the case-study portfolio (the taxonomy is described in Table 1).

Table 7
$E(LR)$ values obtained for all building classes considered in the case-study portfolio.

	Proposed approach	Alternative approach #1	Alternative approach #2
W-LFM-DUL-H2	0.144	0.039	0.121
W-LFM-DUM-H2	0.036	0.007	0.024
W-LFM-DUL-H5	0.214	0.020	0.129
W-LFM-DUM-H5	0.037	0.002	0.020
CR-LFM-DUL-H2	0.687	0.127	0.633
CR-LFM-DUM-H2	0.051	0.011	0.039
CR-LFM-DUL-H5	0.997	0.355	2.072
CR-LFM-DUM-H5	0.719	0.073	0.697
MUR-LWAL-DNO-H2	0.560	0.148	0.529
MUR-LWAL-DNO-H5	0.998	0.569	2.175
MR-LWAL-DUL-H2	0.347	0.090	0.321
MR-LWAL-DUM-H2	0.203	0.051	0.183
MR-LWAL-DUL-H5	0.970	0.368	1.508
MR-LWAL-DUM-H5	0.809	0.190	0.869

a harmonized end-to-end methodology. This methodology includes an innovative procedure (based on the simulated-annealing method) to select ground motions with an approximately uniform distribution of intensity measures that correspond to the characteristics of portfolio assets. The state-dependent fragility model development component leverages the energy-based probabilistic seismic demand model by Gentile and Galasso [28], but also incorporates a collapse probability model. The state-dependent vulnerability model development process relies on damage-to-loss models that are widely available in the literature. State-dependent fragility and vulnerability models are developed for 561 building classes of a global database provided by the Global Earthquake Model (GEM), using corresponding equivalent single-degree-of-freedom numerical models and a candidate ground-motion database comprising of around 7000 multi-component records from active shallow earthquakes.

This study also presents a possible approach for using the developed state-dependent fragility and vulnerability models in portfolio loss assessments that incorporate seismic sequences. The proposed approach quantifies the time-dependent increase in the damage states of assets with the state-dependent fragility models, and estimates corresponding loss ratio increments with the state-dependent vulnerability models. The approach is illustrated with a portfolio of building classes representative of the old Christchurch central business district and ground motions of four earthquakes from the 2010–2012 Canterbury sequence. This approach is compared to two alternative approaches: (a) the conventional approach to seismic loss assessment that only

considers the consequences of the mainshock ground motion; and (b) the approach of (a), but including a memoryless evaluation of damage from aftershocks. Approach (a) is the state-of-practice in portfolio seismic loss assessments. Approach (b) is simpler than the proposed approach, failing to consider typical real-life situations where assets remain unrepaired between events of a sequence. Results reveal that the proposed approach leads to final expected loss ratios two to 20 times higher than those of approach (a). The proposed approach also produces more reasonable results than those of approach (b), which can lead to expected losses that far exceed the replacement value of an asset. These findings underline the importance of a portfolio loss assessment appropriately capturing the time-dependent nature of the built environment's condition throughout a seismic sequence.

In summary, the model development methodology used in this study can support the development of extensive suites of state-dependent fragility and vulnerability models for quantifying the potential impact of damage accumulation in large-scale loss assessments of building portfolios. Although the approach proposed for implementing the developed state-dependent models in portfolio-level seismic risk assessments only captures seismic sequences in this study, it could be extended to account for the time-dependent condition of assets in more complete probabilistic seismic risk analyses. Region-specific models for building repair time could also be integrated into these analyses to realistically describe the cumulative damage of assets that remain unrepaired for years (as in the cases of the 2010–2012 Canterbury and the 2009 L'Aquila sequence; [72,73]).

CRediT authorship contribution statement

Salvatore Iacoletti: Conceptualization, Methodology, Software, Writing – original draft, Writing – review & editing. **Gemma Cremen:** Conceptualization, Methodology, Supervision, Writing – review & editing. **Carmine Galasso:** Conceptualization, Methodology, Supervision, Writing – review & editing.

Declaration of competing interest

The authors declare that they have no known competing financial interests or personal relationships that could have appeared to influence the work reported in this paper.

Data availability

The OpenSees software is available at https://opensees.berkeley.edu/ and https://openseespydoc.readthedocs.io/en/latest/ (last

accessed 18th Mar 2022). Martins and Silva [10]'s capacity curve database is available at https://github.com/lmartins88/global_fragility_vulnerability/ (last accessed 18th Mar 2022). Codes for performing the methodology described in this study are available at https://github.com/SalvIac/pysdvuln and the database of fragility and vulnerability models are available at https://github.com/SalvIac/sequence_frag_vuln. Response spectra of the four considered events from the 2010–2012 Canterbury sequence are available at https://www.geonet.org.nz/ (last accessed 18th Mar 2022).

Acknowledgments

References

[1] Kam WY, Pampanin S, Dhakal R, Gavin HP, Roeder C. Seismic performance of reinforced concrete buildings in the September 2010 Darfield (Canterbury) Earthquake. Bull New Zealand Soc Earthq Eng 2010;43(4):340–50. http://dx.doi.org/10.5459/bnzsee.43.4.340-350.

[2] Kam WY, Pampanin S, Elwood K. Seismic performance of reinforced concrete buildings in the 22 February Christchurch (Lyttelton) Earthquake. Bull New Zealand Soc Earthq Eng 2011;44(4):239–78. http://dx.doi.org/10.5459/bnzsee.44.4.239-278.

[3] Moon L, Dizhur D, Senaldi I, Derakhshan H, Griffith M, Magenes G, et al. The demise of the URM building stock in Christchurch during the 2010–2011 Canterbury earthquake sequence. Earthq Spectra 2014;30(1):253–76. http://dx.doi.org/10.1193/022113EQS044M.

[4] Abdelnaby AE, Elnashai AS. Performance of degrading reinforced concrete frame systems under the Tohoku and Christchurch earthquake sequences. J Earthq Eng 2014;18(7):1009–36. http://dx.doi.org/10.1080/13632469.2014.923796.

[5] Mildon ZK, Roberts GP, Faure Walker JP, Iezzi F. Coulomb stress transfer and fault interaction over millennia on non-planar active normal faults: The Mw 6.5–5.0 seismic sequence of 2016–2017, Central Italy. Geophys J Int 2017;210(2):1206–18. http://dx.doi.org/10.1093/gji/ggx213.

[6] Stewart J, Lanzo G, Ausilio E, Cairo R, Bozzoni F, Capatti MC, et al. Engineering reconnaissance following the October 2016 Central Italy earthquakes - version 2. 2017, http://dx.doi.org/10.18118/G6HS39.

[7] Jalayer F, Cornell CA. A Technical Framework for Probability-Based Demand and Capacity Factor Design (DCFD) Seismic Formats. Pacific Earthquake Engineering Research Center; 2003, p. 122.

[8] Federal Emergency Management Agency P-58-1. Seismic performance assessment of buildings, volume 1 – methodology. 2nd ed.. 2012, p. 340.

[9] D'Ayala D, Meslem A, Vamvatsikos D, Porter K, Rossetto T, Crowley H, et al. GEM guidelines for analytical vulnerability assessment of low/mid-rise buildings. 2014.

[10] Martins L, Silva V. Development of a fragility and vulnerability model for global seismic risk analyses. Bull Earthq Eng 2020. http://dx.doi.org/10.1007/s10518-020-00885-1.

[11] Iervolino I, Giorgio M, Chioccarelli E. Markovian modeling of seismic damage accumulation. Earthq Eng Struct Dyn 2016;45(3):441–61. http://dx.doi.org/10.1002/eqe.2668.

[12] Aljawhari K, Gentile R, Freddi F, Galasso C. Effects of ground-motion sequences on fragility and vulnerability of case-study reinforced concrete frames. Bull Earthq Eng 2020. http://dx.doi.org/10.1007/s10518-020-01006-8.

[13] Shome N, Williams C. Aftershock risk in Japan following Tohoku earthquake. In: Tenth U.S. National Conference on Earthquake Engineering. 2014, p. 11.

[14] Field E, Porter K, Milner K. A prototype operational earthquake loss model for California based on UCERF3-ETAS – a first look at valuation. Earthq Spectra 2017;33(4):1279–99. http://dx.doi.org/10.1193/011817eqs017m.

[15] Papadopoulos AN, Bazzurro P. Exploring probabilistic seismic risk assessment accounting for seismicity clustering and damage accumulation: part II. Risk analysis. Earthq Spectra 2020. http://dx.doi.org/10.1177/8755293020938816.

[16] Luco N, Bazzurro P, Cornell CA. Dynamic versus static computation of the residual capacity of mainshock-damaged building to withstand an aftershock. In: Proceedings 13th world conference on earthquake engineering. Vancouver, B.C., Canada; 2004, p. 16.

[17] Vamvatsikos D, Cornell CA. Incremental dynamic analysis. Earthq Eng Struct Dyn 2002;31(3):491–514. http://dx.doi.org/10.1002/eqe.141.

[18] Raghunandan M, Liel AB, Luco N. Aftershock collapse vulnerability assessment of reinforced concrete frame structures. Earthq Eng Struct Dyn 2015;44(3):419–39. http://dx.doi.org/10.1002/eqe.2478.

[19] Jeon JS, DesRoches R, Lowes LN, Brilakis I. Framework of aftershock fragility assessment–case studies: Older California reinforced concrete building frames. Earthq Eng Struct Dyn 2015;44(15):2617–36. http://dx.doi.org/10.1002/eqe.2599.

[20] Goda K. Record selection for aftershock incremental dynamic analysis. Earthq Eng Struct Dyn 2015;44(7):1157–62. http://dx.doi.org/10.1002/eqe.2513.

[21] Papadopoulos AN, Kohrangi M, Bazzurro P. Mainshock-consistent ground motion record selection for aftershock sequences. Earthq Eng Struct Dyn 2020;49(8):754–71. http://dx.doi.org/10.1002/eqe.3263.

[22] Miano A, Jalayer F, Ebrahimian H, Prota A. Cloud to IDA: efficient fragility assessment with limited scaling. Earthq Eng Struct Dyn 2018;47(5):1124–47. http://dx.doi.org/10.1002/eqe.3009.

[23] Jalayer F. Direct probabilistic seismic analysis: implementing non-linear dynamic assessments. 2003.

[24] Kohrangi M, Bazzurro P, Vamvatsikos D, Spillatura A. Conditional spectrum-based ground motion record selection using average spectral acceleration. Earthq Eng Struct Dyn 2017;46(10):1667–85. http://dx.doi.org/10.1002/eqe.2876.

[25] Jalayer F, Ebrahimian H, Miano A, Manfredi G, Sezen H. Analytical fragility assessment using unscaled ground motion records. Earthq Eng Struct Dyn 2017;46(15):2639–63. http://dx.doi.org/10.1002/eqe.2922.

[26] Zhuang L, Pang Y. Enhanced cloud method (e-cloud) for efficient seismic fragility assessment of structures. 2021, http://dx.doi.org/10.21203/rs.3.rs-647920/v1.

[27] Jalayer F, Ebrahimian H. Seismic risk assessment considering cumulative damage due to aftershocks. Earthq Eng Struct Dyn 2017;46(3):369–89. http://dx.doi.org/10.1002/eqe.2792.

[28] Gentile R, Galasso C. Hysteretic energy-based state-dependent fragility for ground-motion sequences. Earthq Eng Struct Dyn 2021;50(4):1187–203. http://dx.doi.org/10.1002/eqe.3387.

[29] Réveillère A, Gehl P, Seyedi D, Modaressi H. Development of seismic fragility curves for damaged reinforced concrete structures. In: 15th World Conference on Earthquake Engineering. 2012, p. 10.

[30] Hatzigeorgiou GD, Beskos DE. Inelastic displacement ratios for SDOF structures subjected to repeated earthquakes. Eng Struct 2009;31(11):2744–55. http://dx.doi.org/10.1016/j.engstruct.2009.07.002.

[31] Hatzigeorgiou GD, Liolios AA. Nonlinear behaviour of RC frames under repeated strong ground motions. Soil Dyn Earthq Eng 2010;30(10):1010–25. http://dx.doi.org/10.1016/j.soildyn.2010.04.013.

[32] Di Sarno L. Effects of multiple earthquakes on inelastic structural response. Eng Struct 2013;56:673–81. http://dx.doi.org/10.1016/j.engstruct.2013.05.041.

[33] Ruiz-García J, Aguilar JD. Aftershock seismic assessment taking into account postmainshock residual drifts. Earthq Eng Struct Dyn 2015;44(9):1391–407. http://dx.doi.org/10.1002/eqe.2523.

[34] Otárola K, Fayaz J, Galasso C. Fragility and vulnerability analysis of deteriorating ordinary bridges using simulated ground-motion sequences. Earthq Eng Struct Dyn 2022;51(13):3215–40. http://dx.doi.org/10.1002/eqe.3720.

[35] Goda K, Wenzel F, De Risi R. Empirical assessment of non-linear seismic demand of mainshock–aftershock ground-motion sequences for Japanese earthquakes. Front Built Environ 2015;1:6. http://dx.doi.org/10.3389/fbuil.2015.00006.

[36] Porter KA. An overview of PEER's performance-based earthquake engineering methodology. In: Proceedings of Ninth International Conference on Applications of Statistics and Probability in Civil Engineering. 2003, p. 1–8.

[37] Lallemant D, Burton H, Ceferino L, Bullock Z, Kiremidjian A. A framework and case study for earthquake vulnerability assessment of incrementally expanding buildings. Earthq Spectra 2017;33(4):1369–84. http://dx.doi.org/10.1193/011116eqs010m.

[38] Yu X, Zhou Z, Du W, Lu D. Development of fragility surfaces for reinforced concrete buildings under mainshock-aftershock sequences. Earthq Eng Struct Dyn 2021;50(15):3981–4000. http://dx.doi.org/10.1002/eqe.3542.

[39] Kirkpatrick S, Gelatt CD, Vecchi MP. Optimization by simulated annealing. Science 1983;220(4598):671–80. http://dx.doi.org/10.1126/science.220.4598.671.

[40] Xiang Y, Sun DY, Fan W, Gong XG. Generalized simulated annealing algorithm and its application to the thomson model. Phys Lett A 1997;233(3):216–20. http://dx.doi.org/10.1016/S0375-9601(97)00474-X.

[41] Luco N, Bazzurro P. Does amplitude scaling of ground motion records result in biased nonlinear structural drift responses? Earthq Eng Struct Dyn 2007;36(13):1813–35. http://dx.doi.org/10.1002/eqe.695.

[42] Dávalos H, Miranda E. Evaluation of the scaling factor bias influence on the probability of collapse using Sa(T1) as the intensity measure. Earthq Spectra 2019;35(2):679–702. http://dx.doi.org/10.1193/011018EQS007M.

[43] Bianchini M, Diotallevi P, Baker J. Prediction of inelastic structural response using an average of spectral accelerations. In: 10th International Conference on Structural Safety and Reliability. 2009, p. 13–7.

[44] Kohrangi M, Vamvatsikos D, Bazzurro P. Site dependence and record selection schemes for building fragility and regional loss assessment. Earthq Eng Struct Dyn 2017;46(10):1625–43. http://dx.doi.org/10.1002/eqe.2873.

[45] Jalayer F, Beck JL, Zareian F. Analyzing the sufficiency of alternative scalar and vector intensity measures of ground shaking based on information theory. J Eng Mech 2012;138(3):307–16. http://dx.doi.org/10.1061/(ASCE)EM.1943-7889.0000327.

[46] Minas S, Galasso C. Accounting for spectral shape in simplified fragility analysis of case-study reinforced concrete frames. Soil Dyn Earthq Eng 2019;119:91–103. http://dx.doi.org/10.1016/j.soildyn.2018.12.025.

[47] Ruiz-García J. Mainshock-aftershock ground motion features and their influence in building's seismic response. J Earthq Eng 2012;16(5):719–37. http://dx.doi.org/10.1080/13632469.2012.663154.

[48] Tesfamariam S, Goda K, Mondal G. Seismic vulnerability of reinforced concrete frame with unreinforced masonry infill due to main shock–aftershock earthquake sequences. Earthq Spectra 2015;31(3):1427–49. http://dx.doi.org/10.1193/042313EQS111M.

[49] Zhang L, Goda K, Luca FD, Risi RD. Mainshock-aftershock state-dependent fragility curves: A case of wood-frame houses in British Columbia, Canada. Earthq Eng Struct Dyn 2020;49(9):884–903. http://dx.doi.org/10.1002/eqe.3269.

[50] Chun MH, Han SJ, Tak NI. An uncertainty importance measure using a distance metric for the change in a cumulative distribution function. Reliab Eng Syst Saf 2000;70(3):313–21. http://dx.doi.org/10.1016/S0951-8320(00)00068-5.

[51] Richards FJ. A flexible growth function for empirical use. J Exp Bot 1959;10(2):290–301. http://dx.doi.org/10.1093/jxb/10.2.290.

[52] Federal Emergency Management Agency. HAZUS-MH MR5 technical manual-earthquake model. 2010.

[53] Rossetto T, Elnashai A. Derivation of vulnerability functions for European-type RC structures based on observational data. Eng Struct 2003;25(10):1241–63. http://dx.doi.org/10.1016/S0141-0296(03)00060-9.

[54] Iacoletti S, Cremen G, Galasso C. Validation of the epidemic-type aftershock sequence (ETAS) models for simulation-based seismic hazard assessments. Seismol Res Lett 2022. http://dx.doi.org/10.1785/0220210134.

[55] Gentile R, Pampanin S, Galasso C. A computational framework for selecting the optimal combination of seismic retrofit and insurance coverage. Comput-Aided Civ Infrastruct Eng 2021. http://dx.doi.org/10.1111/mice.12778.

[56] Silva V, Amo-Oduro D, Calderon A, Costa C, Dabbeek J, Despotaki V, et al. Development of a global seismic risk model. Earthq Spectra 2020;36(1_suppl):372–94. http://dx.doi.org/10.1177/8755293019899953.

[57] Dolšek M. Simplified method for seismic risk assessment of buildings with consideration of aleatory and epistemic uncertainty. Struct Infrastruct Eng 2012;8(10):939–53. http://dx.doi.org/10.1080/15732479.2011.574813.

[58] McKenna F. OpenSees: A framework for earthquake engineering simulation. Comput Sci Eng 2011;13(04):58–66. http://dx.doi.org/10.1109/MCSE.2011.66.

[59] Abdelnaby AE, Elnashai AS. Numerical modeling and analysis of RC frames subjected to multiple earthquakes. Earthq Struct 2015;9(5):957–81. http://dx.doi.org/10.12989/EAS.2015.9.5.957.

[60] Hosseinpour F, Abdelnaby A. Effect of different aspects of multiple earthquakes on the nonlinear behavior of RC structures. Soil Dyn Earthq Eng 2017;92:706–25. http://dx.doi.org/10.1016/j.soildyn.2016.11.006.

[61] Crowley H, Dabbeek J, Despotaki V, Rodrigues D, Martins L, Silva V, Romão X, Pereira N, Weatherill G, Danciu L. European seismic risk model (ESRM20). EFEHR; 2021, http://dx.doi.org/10.7414/EUC-EFEHR-TR002-ESRM20.

[62] Gentile R, Galasso C. Simplicity versus accuracy trade-off in estimating seismic fragility of existing reinforced concrete buildings. Soil Dyn Earthq Eng 2021;144:106678. http://dx.doi.org/10.1016/j.soildyn.2021.106678.

[63] Mitchell-Wallace K, editor. Natural catastrophe risk management and modelling: A practitioner's guide. Hoboken, NJ: John Wiley and Sons, Inc; 2017.

[64] Bozorgnia Y, Abrahamson NA, Atik LA, Ancheta TD, Atkinson GM, Baker JW, et al. NGA-West2 Research Project. Earthq Spectra 2014;30(3):973–87. http://dx.doi.org/10.1193/072113EQS209M.

[65] Faccioli E, Paolucci R, Rey J. Displacement spectra for long periods. Earthq Spectra 2004;20(2):347–76. http://dx.doi.org/10.1193/1.1707022.

[66] Chopra AK. Dynamics of structures: theory and applications to earthquake engineering. Pearson always learning, 5th ed.. Hoboken, NJ: Pearson; 2017.

[67] Spence R, Martínez-Cuevas S, Baker H. Fragility estimation for global building classes using analysis of the Cambridge Earthquake Damage Database (CEQID). Bull Earthq Eng 2021;19(14):5897–916. http://dx.doi.org/10.1007/s10518-021-01178-x.

[68] Bradley BA, Quigley MC, Van Dissen RJ, Litchfield NJ. Ground motion and seismic source aspects of the Canterbury earthquake sequence. Earthq Spectra 2014;30(1):1–15. http://dx.doi.org/10.1193/030113EQS060M.

[69] Iacoletti S, Cremen G, Galasso C. Integrating long and short-term time dependencies in simulation-based seismic hazard assessments. Earth Space Sci 2022;9(9). http://dx.doi.org/10.1029/2022EA002253, e2022EA002253.

[70] Uma SR, Dhakal RP, Nayyerloo M. Vulnerability assessment of Christchurch buildings in Canterbury earthquakes. Technical report, 2013, p. 35.

[71] NZS 11705. Structural design actions part 5: Earthquake actions-New Zealand. 2004, p. 82, Wellington, New Zealand: Standards New Zealand.

[72] Gjerde M. Building back better: Learning from the Christchurch rebuild. Procedia Eng 2017;198:530–40. http://dx.doi.org/10.1016/j.proeng.2017.07.108.

[73] Contreras D, Forino G, Blaschke T. Measuring the progress of a recovery process after an earthquake: The case of L'Aquila, Italy. Int J Disaster Risk Reduct 2018;28:450–64. http://dx.doi.org/10.1016/j.ijdrr.2017.09.048.